University of Dundee

Imidazo[1,2-b]pyridazines as inhibitors of DYRK kinases

Henderson, Scott H.; Sorrell, Fiona J.; Bennett, James M.; Fedorov, Oleg; Hanley, Marcus T.; Godoi, Paulo H.

[Link to publication in Discovery Research Portal](#)

Research paper

Imidazo[1,2-b]pyridazines as inhibitors of DYRK kinases

Scott H. Henderson [a,*], Fiona J. Sorrell [b], James M. Bennett [c], Oleg Fedorov [b], Marcus T. Hanley [g],
Paulo H. Godoi [f], Roberta Ruela de Sousa [f], Sean Robinson [d], Iva Hopkins Navratilova [d,e],
Jonathan M. Elkins [b,f,**], Simon E. Ward [g,***]

[a] *Sussex Drug Discovery Centre, University of Sussex, Brighton, BN1 9RH, UK*
[b] *Centre for Medicines Discovery, Nuffield Department of Medicine, University of Oxford, Oxford, OX3 7DQ, UK*
[c] *Target Discovery Institute, University of Oxford, Oxford, OX3 7FZ, UK*
[d] *Exscientia, The Schrödinger Building, Oxford Science Park, Oxford, OX4 4GE, UK*
[e] *University of Dundee, Dow Street, Dundee, DD1 5EH, UK*
[f] *Structural Genomics Consortium, Universidade Estadual de Campinas, Cidade Universitária Zeferino Vaz, Av. Dr. André Tosello, 550, Barão Geraldo, Campinas, SP, 13083-886, Brazil*
[g] *Medicines Discovery Institute, Cardiff University, CF10 3AT, UK*

ARTICLE INFO

ABSTRACT

Selective inhibitors of DYRK1A are of interest for the treatment of cancer, Type 2 diabetes and neurological disorders. Optimization of imidazo [1,2-b]pyridazine **fragment 1** through structure−activity relationship exploration and *in silico* drug design efforts led to the discovery of **compound 17** as a potent cellular inhibitor of DYRK1A with selectivity over much of the kinome. The binding mode of **compound 17** was elucidated with X-ray crystallography, facilitating the rational design of **compound 29**, an imidazo [1,2-b]pyridazine with improved kinase selectivity with respect to closely related CLK kinases.

1. Introduction

Post-translational modification through phosphorylation of serine, threonine and tyrosine residues by protein kinases is fundamental to the regulation of all major cellular processes. Aberrant phosphorylation can result in diseases of the central nervous system, inflammatory diseases, auto-immune diseases and cancer. Consequently, protein kinases have become a major therapeutic target in the search for novel treatments for diseases [1].

Dual-specificity tyrosine-phosphorylation-regulated kinases (DYRK) are a family of highly conserved serine-threonine kinases, belonging to the CMGC group of kinases. There are five members of the human DYRK subfamily, further divided into two classes: class I and class II DYRKs [2]. Class II DYRKs, DYRK2, DYRK3 and DYRK4, have been less extensively studied compared to class I DYRKs. Inhibition of DYRK2 has been investigated as a potential treatment for certain types of cancer, owing to DYRK2's role in tumour progression [3,4]. DYRK3 has been identified as a potential negative regulator of erythropoiesis and DYRK3

antagonists have been investigated as a possible therapy for anemia [5, 6]. The biological function of DYRK4 and its role in disease pathogenesis is yet to be established [2].

DYRK1A and DYRK1B (class I), have received the most attention as potential therapeutic targets. The overexpression of DYRK1B in certain tumour types and its identification as a probable oncogene has led to the investigation of DYRK1B inhibitors for the treatment of cancer [2,7]. The roles of DYRK1B in adipogenesis, glucose homeostasis and cancer has resulted in efforts to find isoform selective inhibitors of DYRK1B [8]. DYRK1A controls several pathways that augment cancer cell proliferation, migration and metastasis, encourage resistance to cell death and suppress cellular responses to anti-cancer therapies [9–11]. Atypical expression of DYRK1A is associated with neurodegenerative disorders such as Down's syndrome, Alzheimer's, Parkinson's and Huntington's diseases as well as mental retardation [9]. Recently, DYRK1A inhibition has been shown to promote human beta-cell proliferation [12], which over time can increase glucose-dependent insulin secretion [13,14], highlighting the potential of DYRK1A inhibitors as novel treatments for

---

metabolic disorders such as diabetes and obesity [15]. Furthermore, DYRK1A is a modulator of the Wnt pathway and is being investigated as a novel treatment for osteoarthritis [16]. The field of DYRK1A antagonists has been extensively reviewed [9,17–20].The first inhibitors described were harmine [21] and epigallocatechin gallate [22]. These natural products have inherent problems including the presence of toxic alerts, potent MAO inhibition, lack of selectivity and poor *in vivo* ADME properties. Over recent years, many researchers have attempted to find proof-of-concept tools and more drug-like DYRK1A inhibitors. A limited number of these molecules have been validated as DYRK1A inhibitors in disease relevant models *in vivo* [23–28] and fewer have advanced to clinical development [29–35].

The discovery of a drug-like, isoform selective DYRK1A inhibitor has so far proven elusive. DYRK1A and DYRK1B share 85% sequence homology and differ by 1 amino acid on the hinge region of the ATP site. In the case of tumour progression, the class I DYRKs appear to have confounding roles [2]. Given the genotoxicity concerns of dual inhibition with CLKs and other closely related CMGC kinases [36], especially if the molecule is intended for an indication other than oncology, it remains desirable to discover an isoform selective inhibitor of DYRK1A. Encouragingly two FDA-approved kinase inhibitors, silmitasertib and abemaciclib, inhibit DYRK1A as effectively as their primary kinase targets, suggesting that DYRK1A inhibition through pharmacological intervention is tolerated in humans (Fig. 1) [37,38].

2. Results and discussion

2.1. Compound design

Fragment **1** was discovered whilst exploring imidazo [1,2-*b*]pyridazines as a potential series for kinase inhibition. **1** showed promise for fragment growing due to its ease of synthetic elaboration, attractive ligand efficiency, favorable thermodynamic solubility and low intrinsic clearance when tested in human liver microsomes (Fig. 2). Imidazo [1,2-*b*]pyridazines have been reported to possess DYRK1/CLK inhibitory activity [39,40]. In 2017 Bendjeddou et al. discovered a series of 3, 6-disubstituted imidazo [1,2-*b*]pyridazines that had dual DYRK/CLK activity [39]. Despite the lack of structural information on the binding mode of the series reported, we were confident that an increase in DYRK1A binding affinity would be achieved from exploring the C-3 position of fragment **1**. This would likely lead to a simultaneous increase

in the binding affinity for the CLK family of kinases, in line with the findings of Bendjeddou et al. [39] Previously, our research group identified a series of pyrazolo [1,5-*b*]pyridazines that were isoform selective inhibitors of DYRK1A [44,45]. Selectivity against close off-targets, such as the CLKs and DYRK1B, was achieved by occupying a shallow lipophilic cleft unique to the hinge of DYRK1A with a methyl substituent. We envisaged that we could increase the potency of fragment **1** by exploring the C3-position and then improve kinase selectivity guided by structure-based drug design. Here we present our efforts in the development of the imidazo [1,2-*b*]pyridazine scaffold as potent and selective DYRK1A kinase inhibitors, including both structural and selectivity analysis.

2.2. Chemistry

We chose to explore, in parallel, (i) the 5,6-heterocyclic core of fragment **1**; (ii) the 2-position of the imidazo [1,2-*b*]pyridazine core; (iii) the 6-position of the imidazo [1,2-*b*]pyridazine core; and (iv) the 3-position of the imidazo [1,2-*b*]pyridazine core. Synthetic strategies were devised to investigate these four aspects of the series. The majority of 5,6-heterocycles were accessed following Suzuki protocol under mild conditions with commercially available heterocyclic halides and 4-pyridyl boronic acid (Scheme 1).

Substituents were installed in the 2 position of the imidazo [1,2-*b*] pyridazine fragment in two steps: Suzuki reaction with 4-pyridyl boronic acid on 6-chloropyridazin-3-amine afforded key intermediate **I-1**. Subsequent cyclisation with α-haloketone furnished the desired 2-substituted imidazo [1,2-*b*]pyridazines. Reversing the sequence of synthetic steps in the case of compound **4** gave superior yields in the exploration of the 2-position (Scheme 2).

To complete the methyl scan of the imidazo [1,2-*b*]pyridazine core, the 7- and 8- positions were accessed from a common starting material. Heating 3,6-dichloro-4-methylpyridazine with aminoacetaldehyde dimethyl acetal followed by sulfuric acid gave a 2:1 mixture of **I-3:I-4**, which were separable by conventional chromatography. The 4-pyridyl motif was installed at the 6-position under familiar Suzuki protocol to afford compounds **7** and **8** (Scheme 3).

The 3-position was fixed as 3-(trifluoromethoxy)phenyl and the 6-position of the imidazo [1,2-*b*]pyridazine core was explored. Tandem Suzuki reactions provided rapid access to an array of 3,6-diaryl imidazo [1,2-*b*]pyridazines. Starting with 3-bromo-6-chloroimidazo [1,2-*b*]
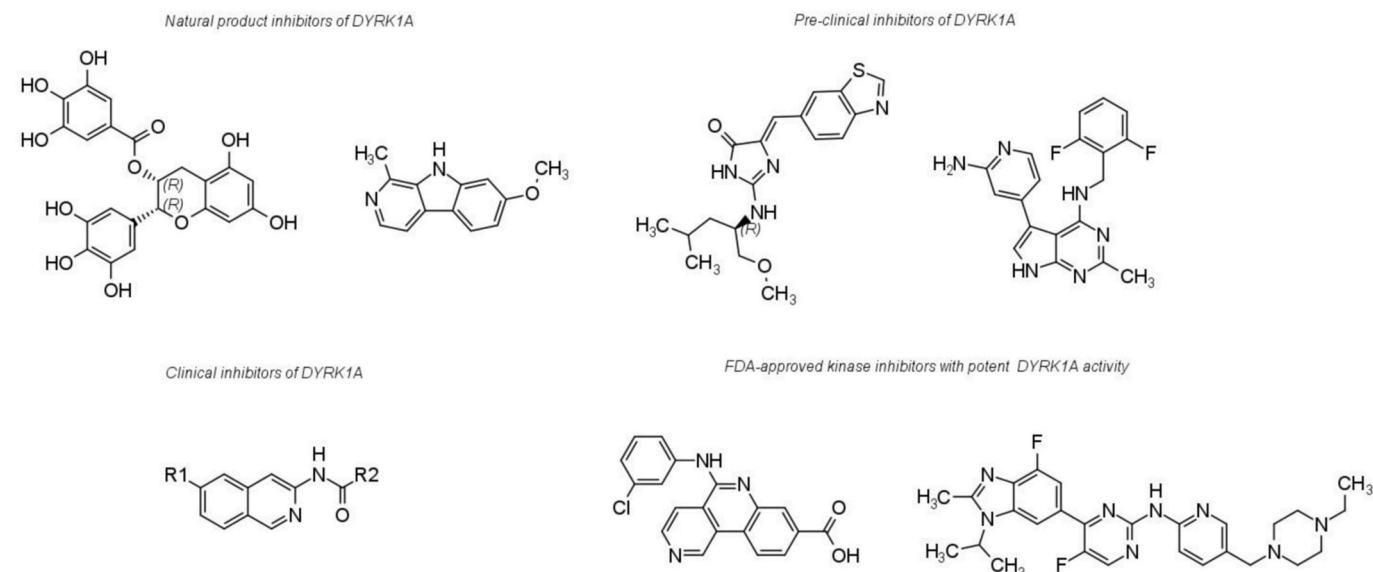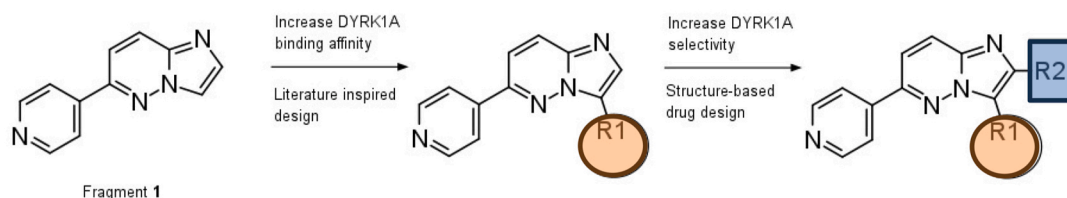

Fig. 1. Natural product inhibitors of DYRK1A: ECGC and harmine; DYRK1A pre-clinical compounds Leucettinib-21 and Servier-Vernalis compound 34; The Markush of clinical DYRK1A inhibitor SM07783; FDA approved kinase inhibitors that possess potent DYRK1A inhibitory activity: silmitasertib and abemaciclib.

Compound design strategy

Fragment 1

Fragment 1 profile

Compound	Structure	DYRK1A IC$_{50}$	LE	HLM ((μg/(min mg))	Solubility (μM)
1		2640	0.52	12 ± 2	> 250

[a]IC$_{50}$ (nM) in TR-FRET-based ligand-binding displacement assay measured with two technical replicates (n = 1 biological replicate). LE = 1.4(pIC$_{50}$)/non-hydrogen atoms. HLM and RLM determinations mean of n = 2 ± standard deviation (unless otherwise stated). HLM = human liver microsomes, RLM = rat liver microsomes; thermodynamic solubility data was derived from a single experiment at pH 6.8.

Fig. 2. Medicinal chemistry strategy to (i) improve DYRK1A binding affinity and (ii) improve the selectivity of fragment **1**.
[a]IC$_{50}$ (nM) in TR-FRET-based ligand-binding displacement assay measured with two technical replicates (n = 1 biological replicate). LE = 1.4 (pIC$_{50}$)/non-hydrogen atoms. HLM and RLM determinations mean of n = 2 ± standard deviation (unless otherwise stated). HLM = human liver microsomes, RLM = rat liver microsomes; thermodynamic solubility data was derived from a single experiment at pH 6.8.
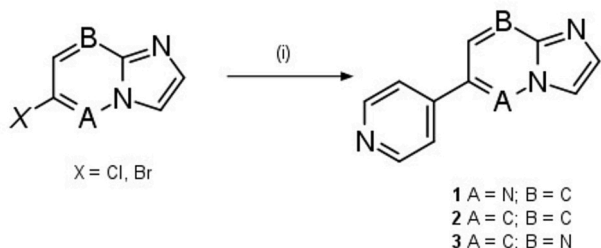
Scheme 1. Reagents and conditions: (a) Pyridine-4-boronic acid hydrate, bis [2-(di-tert-butylphosphanyl)cyclopenta-2,4-dien-1-yl]iron; dichloropalladium, Cs$_2$CO$_3$ or Na$_2$CO$_3$, water/MeCN (1:10), 80 °C, 16 h, 30–48% yield.

pyridazine, and taking advantage of the increased reactivity of the bromo substituent to cross-coupling, a Suzuki reaction was performed to selectively install 3-(trifluoromethoxy)phenyl substituent, **I-5**. Subsequent microwave-promoted Suzuki reaction installed the second aryl group at the 6-position to furnish the desired 3,6-diaryl imidazo [1,2-*b*] pyridazines **9**–**22**. Compound **25** was delivered by ambient temperature hydrogenation of the unsaturated tetrahydropyran motif of compound **24**. Buchwald-Hartwig amination of **I-5** with morpholine gave compound **26** in acceptable yield (Scheme 4).

Selective exploration of the 3-position required a modular approach: key intermediate **I-6** was accessed via electrophilic bromination of fragment **1** with *N*-bromosuccinimide. Suzuki reaction between intermediate **I-6** and 3,6-dihydro-2*H*-pyran-4-boronic acid pinacol ester under microwave irradiation afforded unsaturated derivative **27**. Subsequent reduction of the alkene double bond proved difficult at first and required catalytic transfer hydrogenation with ammonium formate at

elevated temperature to afford compound **28** (Scheme 5).

Compound **29** was synthesized using a similar procedure as outlined previously. Bromination of compound **4** followed by Suzuki protocol with prolonged heating, furnished compound **29** (Scheme 6).

To reduce the potential for π-stacking and aqueous insolubility, we attempted to replace the lipophilic 3-(trifluoromethoxy)-phenyl group with more polar groups that possessed sp^3 character. Solubilizing motifs were appended to the 3-position of the imidazo [1,2-*b*]pyridazine scaffold via a high-yielding acid-catalysed Mannich reaction on **I-2**, followed by familiar Suzuki protocol (Scheme 7).

2.3. X-ray crystallography

The co-crystal structure of **17**:DYRK1A was determined by X-ray crystallography (PDB code 6S11) showing **17** bound in the ATP site of DYRK1A in Type I fashion [41]. A hydrogen bond from the pyridyl N atom to the catalytic Lys 188 was clearly present. A second hydrogen bond is formed between the imidazo N of the core and Leu241 hinge residue. A non-classical H bond is potentially formed between the aromatic C-H of the imidazo [1,2-*b*]pyridazine core and the carbonyl of Glu 239 at the hinge of DYRK1A. The lipophilic 3-(trifluoromethoxy)-phenyl motif sits beneath the glycine rich P-loop (Fig. 3).

2.4. DYRK1A TR-FRET binding assay

In vitro binding affinities of imidazo [1,2-*b*]pyridazines against DYRK1A were evaluated using a TR-FRET based assay with staurosporine as a reference standard. The binding affinities of compounds **1**–**8** are listed in Table 1. Scaffold-hopping to imidazo [1,2-*a*]pyridine **2** and imidazo [1,2-*a*]pyrimidine **3** increased DYRK1A binding affinity
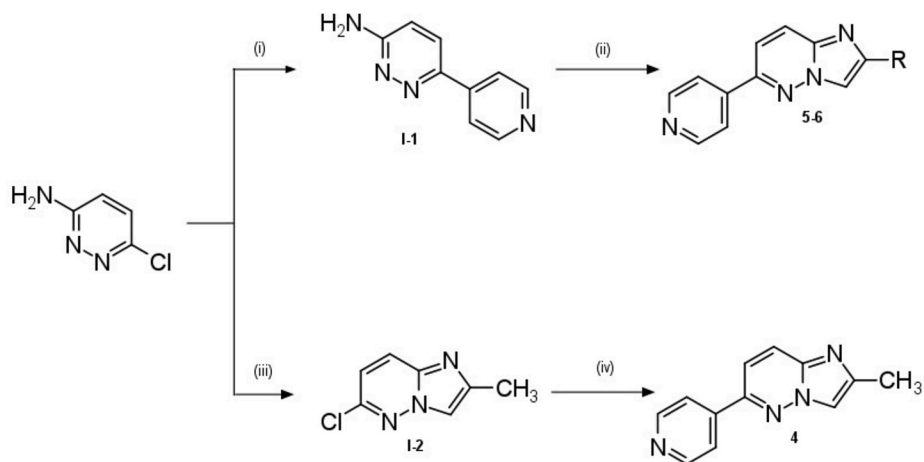
**Scheme 2.** Reagents and conditions: (i) Pyridine-4-boronic acid hydrate, bis(triphenylphosphine)palladium (II)dichloride, potassium phosphate tribasic, water/n-BuOH (3:12), 130 °C, 16 h, 20% yield; (ii) α-haloketone, triethylamine, ethanol, 150 °C, 1.5–16 h, 6–12% yield; (iii) chloroacetone, triethylamine, ethanol, 1 h, 87% yield; (iv) Pyridine-4-boronic acid hydrate, bis [2-(di-tert-butylphosphanyl)cyclopenta-2,4-dien-1-yl]iron; dichloropalladium, Na_2CO_3, water/MeCN (1:10), 80–140 °C, 16 h, 71% yield.
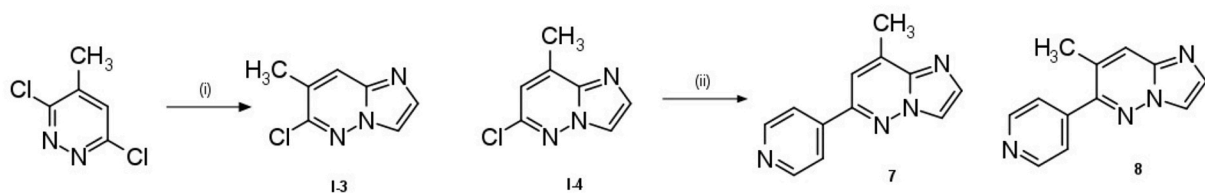
Scheme 3. Reagents and conditions: (i) Aminoacetaldehyde dimethyl acetal, 100 °C, 4 h, then sulfuric acid, 100 °C, 1 h, 20–40% yield; (ii) pyridine-4-boronic acid hydrate, bis [2-(di-tert-butylphosphanyl)cyclopenta-2,4-dien-1-yl]iron; dichloropalladium, K_2CO_3, water/ethanol (0.4/1.6), 120 °C, 21–62 min, μwave, 45–66% yield.
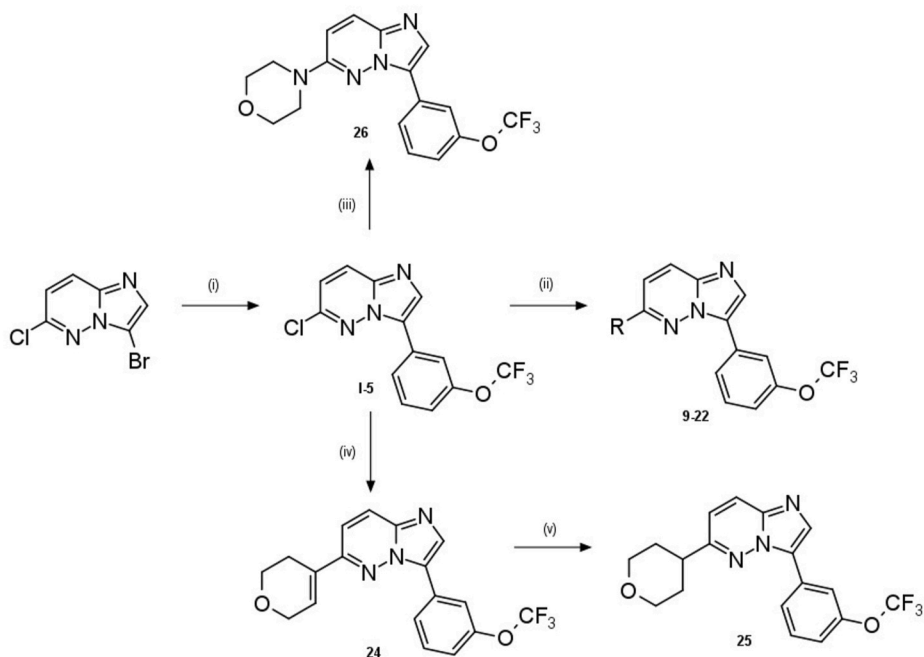
Scheme 4. Reagents and conditions: (i) [3-(Trifluoromethoxy)phenyl]boronic acid, Pd (dppf)Cl_2, Cs_2CO_3, water/1,4-dioxane (1:6), 110 °C, 16 h, 56% yield; (ii) RB (OH)$_2$, Pd(PPh$_3$)$_2$Cl$_2$, Na_2CO_3, water/MeCN (1:5), 120–150 °C, 15–30 min, μwave, 29–80% yield; or RB(OH)$_2$, bis [2-(di-tert-butylphosphanyl)cyclopenta-2,4-dien-1-yl]iron; dichloropalladium, Cs_2CO_3, water/MeCN (1:4), 140 °C, 20 min, μwave, 24–53% yield; (iii) Morpholine, Pd(OAc)$_2$, XPhos, NaOH, 1,4-dioxane, 90 °C, 48 h, 25% yield; (iv) 3,6-dihydro-2H-pyran-4-boronic acid pinacol ester, bis [2-(di-tert-butylphosphanyl)cyclopenta-2,4-dien-1-yl]iron; dichloropalladium, K_2CO_3, water/MeCN (1:6), 140 °C, 25 min, μwave, 62% yield; (v) Palladium on carbon (10% wetted with water), hydrogen balloon, ethanol, rt, 94% yield.
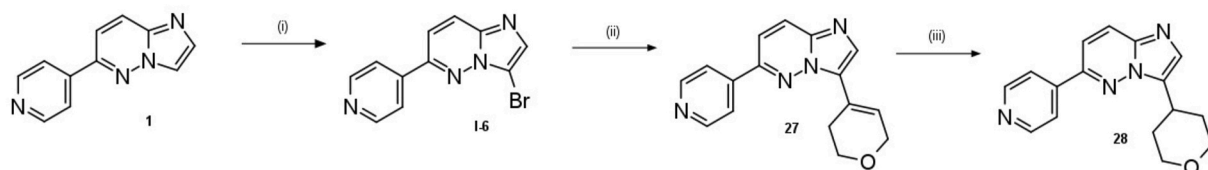
Scheme 5. Reagents and conditions: (i) N-bromosuccinimide, chloroform, rt, 16 h, 51% yield (ii). 3,6-dihydro-2H-pyran-4-boronic acid pinacol ester, bis [2-(di-tert-butylphosphanyl)cyclopenta-2,4-dien-1-yl]iron; dichloropalladium, $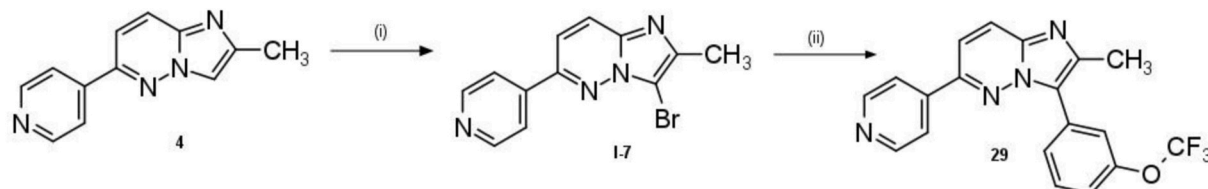K_2CO_3$, water/MeCN (1:6), 140 °C, 25 min, μwave, 41% yield; (iii) Palladium on carbon (10% wetted with water), ammonium formate, ethanol, 75 °C, 32 h, 22% yield.

Scheme 6. Reagents and Conditions; (i) N-bromosuccinimide, DMF, rt, 16 h, 66% yield; (ii) [3-(trifluoromethoxy)phenyl]boronic acid, bis [2-(di-tert-butylphosphanyl)cyclopenta-2,4-dien-1-yl]iron; dichloropalladium, cesium carbonate, acetonitrile:water (8:1), 110 °C, 48 h, 59% yield.
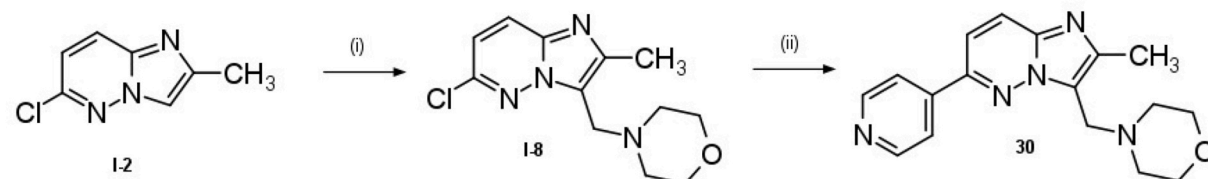
Scheme 7. Reagents and Conditions; (i) Morpholine, formaldehyde solution, acetic acid, methanol, 65 °C, 16 h, 90% yield; (ii) Pyridine-4-boronic acid hydrate, bis [2-(di-tert-butylphosphanyl)cyclopenta-2,4-dien-1-yl]iron; dichloropalladium, potassium carbonate, acetonitrile (3.2:0.8), 120 °C, 21 min, μwave, 41% yield.
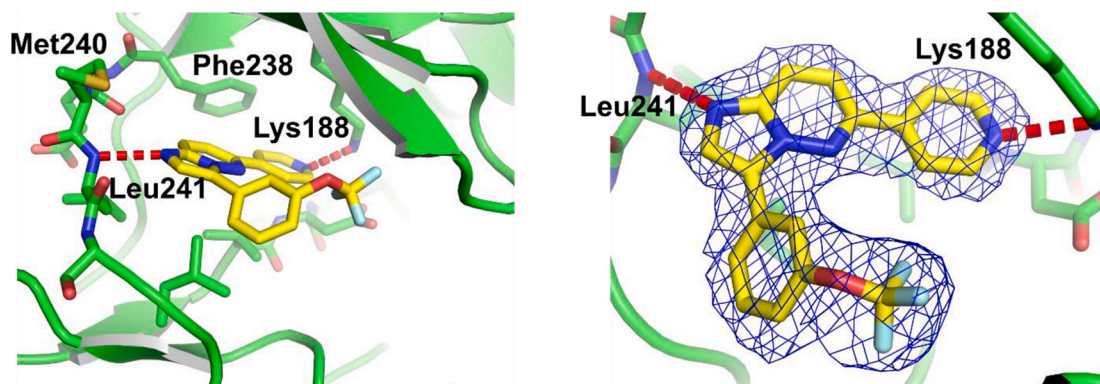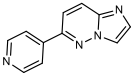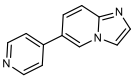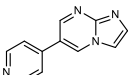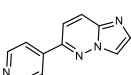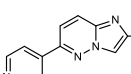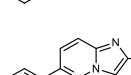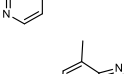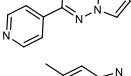

Fig. 3. Co-crystal structure of **17** with DYRK1A (PDB 6S11). On the left compound **17** can be seen bound in the ATP-binding site of DYRK1A forming a hydrogen bond with the kinase hinge region at Leu241. On the right a view from an alternative angle showing the experimental electron density as a 2*Fo-Fc* map contoured at 1.0σ around compound **17**.

relative to fragment **1**. Imidazo [1,2-*a*]pyrimidines are susceptible to Dimroth rearrangements under certain reaction conditions, which can lead to structural misassignment [42]. To a lesser extent, rearrangements of imidazo [1,2-*a*]pyridines are known in the presence of some electron withdrawing substituents at the C-6 position [43]. To build reliable SAR, the decision was taken to focus expansion on fragment **1**. Methylation of the 2-position of the imidazo [1,2-*b*]pyridazine core to give compound **4** improved DYRK1A binding affinity, L.E and L.L.E relative to fragment **1**. Encouraged by this result, other substituents were investigated in the 2-position of the imidazo [1,2-*b*]pyridazine core. Larger substituents (compounds **5** and **6**) were not tolerated in the 2-position. Methyl substituents were not tolerated in positions 7 and 8

(compounds **7** and **8**) of the imidazo [1,2-*b*]pyridazine core. Inspection of the co-crystal structure of **17**:DYRK1A (Fig. 3) reveals that substituents at the 7 and 8 positions of the imidazo [1,2-*b*]pyridazine scaffold are likely to cause steric clashes, detrimental to binding affinity, due to their close proximity to the hinge amino acid residues of DYRK1A. It was found that transposing the 3-(trifluoromethoxy)phenyl substituent from the 2-position to the 3-position enhanced the binding affinity of compound **17** by a factor of 1000 relative to compound **6** (Table 2).

With robust synthetic routes in-hand, a small array of 3-(trifluoromethoxy)phenyl imidazo [1,2-*b*]pyridazines were synthesized and the biological results are shown in Table 2. Of the examples synthesized the 4-pyridyl analogue **17** bound to DYRK1A with the strongest affinity.

Table 1
Scaffold exploration.

Compound	R	DYRK1A IC$_{50}$[a]	clog P	LE	LLE
1		2640	1.47	0.52	4.11
2		149	1.19	0.68	5.64
3		513	0.24	0.59	6.06
4		419	1.60	0.60	4.80
5		**	2.73	0	0
6		>1000000	4.63	0	0
7		>1000000	1.98	0	0
8		**	1.98	0	0

[a] IC$_{50}$ (nM) in TR-FRET-based ligand-binding displacement assay measured with two technical replicates (n = 1 biological replicate). LE = 1.4 (pIC$_{50}$)/non-hydrogen atoms. LLE = pIC50 − clog P.**data did not fit curve.

The position of the pyridyl nitrogen proved crucial for DYRK1A inhibitory activity (c.f. Compound **17** vs compound **18**). Addition of a methyl substituent at the 2 or 3 position of the 4-pyridyl motif were tolerated. In general, the LLE of the imidazo [1,2-*b*]pyridazine series is below 3. Preparation of saturated heterocyclic analogues that possess a heteroatom in a similar position as compound **17**, such as morpholine **26** and tetrahydropyran analogues **24** and **25**, were explored. Substitution of the 4-pyridyl motif led to reductions in potency across the board, compounds **24–26** did not preserve DYRK1A binding affinity, suggesting that it would be difficult to mimic the interaction of the 4-pyridyl moiety with a saturated system. Complete removal of the 4-pyridyl substituent (compound **23**) showed that the 3-(trifluoromethoxy)-phenyl group was not the major contributor to binding affinity. It was evident that SAR was restrictive around the 4-pyridyl motif (Tables 1 and 2).

Substitution of the 3-(trifluoromethoxy)-phenyl group with a more saturated system, such as tetrahydropyran derivatives **27** and **28** led to improvements in LE and LLE, suggesting that the 3-position could be utilized further for optimization of the physical properties of the series without being overly detrimental to DYRK1A binding affinity (compound **27**) (Table 3).

After overlaying the X-ray crystal structures of compound **17** with selective pyrazolo [1,5-*b*]pyridazine DYRK1A inhibitors reported previously by our group [44,45], (supplementary information, SI Fig. 1) we hypothesized that adding a small lipophilic moiety to the 2 position of the imidazo [1,2-*b*]pyridazines may result in an improvement in kinase selectivity. Furthermore, improvements in binding affinity had been observed H < Me for compounds **1** and **4** (Table 1). The methyl substituent added to the 2-position (compound **29**) was well tolerated and evidently small enough to be accommodated in the 'selectivity' cleft present at the hinge region of DYRK1A [45]. Disappointingly, all Mannich products, designed to improve the physical properties of the series and exemplified by compound **30**, exhibited diminished DYRK1A

binding affinity and were not advanced to solubility or metabolic stability studies (Table 4).

2.5. Inhibitor selectivity

2.5.1. Radiometric activity assay (^{33}PanQinase® Activity Assay)

A representative selection of compounds from the imidazo [1,2-*b*]pyridazine series were profiled in a radiometric kinase assay (^{33}PanQinase® Activity Assay) provided by Proqinase GmbH. The assay measured the kinase activity of CMGC kinases (DYRK1A, GSK3β and CDK2) in the presence and absence of inhibitors at 1 μM concentration. Staurosporine was used as a positive control (Table 5).

In addition to inhibiting DYRK1A as predicted from our binding data, compound **17** also inhibits CDK2 to some extent. Flanking the 4-pyridyl substituent (compound **21**) or adding a substituent at the 2-position of the 4-pyridyl ring (compound **19**) removes CDK2 activity albeit with some loss to DYRK1A inhibitory activity. In contrast to other chemotypes that inhibit DYRK1A [45], this class of imidazo [1,2-*b*]pyridazines appears not to inhibit GSK3β (Table 5).

2.5.2. Thermal shift selectivity profiling of compound 17

To profile the selectivity of the series further, **17** was screened at 10 μM for the ability to affect the melting temperature of a panel of 48 kinases using a differential scanning fluorimetry (DSF) assay. The difference in denaturation temperature of kinase protein (δTm) in the presence and absence of an inhibitor is predictive of compound affinity [46]. Staurosporine was used as a positive control. A summary of the selectivity of **17** is shown in Table 6 (complete dataset is available in supplementary information and names of the 48 kinases is included in the Materials and Methods section). Around a third of the kinases tested in the panel exhibited a positive δTm, giving an early indication that compound **17** required further optimization in terms of selectivity

Table 2

3-(trifluoromethoxy)phenyl imidazo [1,2-b]pyridazines.
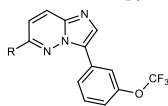
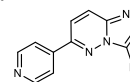| Compound	R	DYRK1A IC$_{50}$[a]	clog P	LE	LLE
9		9999	5.68	0.27	0
10		70000	5.53	0.21	0
11		2020	5.31	0.27	0.38
12		13200	5.56	0.24	0
13		2470	4.54	0.28	1.07
14		>1000000	5.54	0	0
15		>1000000	6.29	0	0
16		>1000000	6.56	0	0
17		25	4.47	0.41	3.13
18		1850	4.47	0.31	1.26
19		259	4.98	0.30	1.62
20		37800	4.31	0.22	0.11
21		96	4.60	0.36	2.42
22		584	4.90	0.31	1.33
23		18000	3.65	0.30	1.09
24		180	4.35	0.40	2.35
25		1450	4.20	0.30	1.60
26		579	4.14	0.30	2.09

[a] IC$_{50}$ (nM) in TR-FRET-based ligand-binding displacement assay measured with two technical replicates (n = 1 biological replicate). LE = 1.4 (pIC$_{50}$)/non-hydrogen atoms. LLE = pIC50 − clog P.

(Table 6).

2.5.3. KinomeSCAN profiling of compound 17

The broader kinome selectivity of compound **17** was determined

Table 3

6-(4-pyridyl) imidazo [1,2-b]pyridazines.

Compound	R	DYRK1A IC$_{50}$[a]	clog P	LE	LLE
27		123	1.70	0.56	5.21
28		815	1.73	0.40	4.37

[a] IC$_{50}$ (nM) in TR-FRET-based ligand-binding displacement assay measured with two technical replicates (n = 1 biological replicate). LE = 1.4 (pIC$_{50}$)/non-hydrogen atoms. LLE = pIC50 − clog P.

Table 4

4-{2-methylimidazo[1,2-b]pyridazin-6-yl}pyridines.

Compound	R	DYRK1A IC$_{50}$[a]	clog P	LE	LLE
29		28	4.60	0.39	2.96
30		5370	1.24	0.30	4.10

[a] IC$_{50}$ (nM) in TR-FRET-based ligand-binding displacement assay measured with two technical replicates (n = 1 biological replicate). LE = 1.4 (pIC$_{50}$)/non-hydrogen atoms. LLE = pIC50 − clog P.

Table 5

CMGC Selectivity of selected imidazo [1,2-b]pyridazines.

Compound	DYRK1A[a]	GSK3β[a]	CDK2[a]
17	93	0	41
19	43	0	11
21	60	0	10
26	32	3	9

[a] % inhibition in[33]PanQinase® Activity Assay (n = 1).

Table 6

DSF Selectivity of selected imidazo [1,2-b]pyridazines.

Compound	% of panel for which positive δ Tm values observed + > 1 °C shift	Kinases for which highest positive δ Tm values observed
17	15/48 (31%)	AAK1, BMP2K, CLK1, GSG2A

with the KINOMEscan assay panel (DiscoverX). Percentage inhibition data for CMGC kinases regularly inhibited by DYRK1A inhibitors reported in the literature are summarized in Table 7 (the full dataset is available in the supplementary information). Compound **17** represents a relatively selective inhibitor of DYRK1A, with a selectivity score (35) = 0.136. Isoforms DYRK1B and DYRK2, in addition to other closely related CMGC kinases, such as the CLKs and haspin are the top off-targets of the imidazo [1,2-*b*]pyridazine series (Table 7), consistent with the DSF results.

2.5.4. Biolayer interferometry (BLI) CMGC panel profiling of compound 29

The kinome selectivity of compound **29** was expected to be improved

Table 7
KINOMEscan Selectivity Profiling of compound **17**.

Kinase	Compound 17
DYRK1A	100
DYRK1B	99.7
DYRK2	89
CLK1	98.6
CLK2	100
CLK3	80
Haspin	94.6
S Score (35)	0.136

[a] % inhibition at 1 μM inhibitor concentration determined in competition binding assay (DiscoverX, n = 1).

relative to compound **17** as a result of adding the 2-methyl substituent to the imidazo [1,2-*b*]pyridazine core. The BLI results indicated that compound **29** showed improved selectivity against CLK1, compared to compound **17** (Table 8).

2.6. Cellular activity of compound 17

Compound **17** was tested for direct binding to DYRK1A in live cells using a NanoBRET target engagement assay (Fig. 4). Compound **17** demonstrated potent cellular activity, with IC_{50} of 41 nM (competing against 1 μM tracer) or 50 nM (competing against 2 μM tracer) compared to the *in vitro* IC_{50} of 25 nM (pIC_{50} = 7.60, Table 2).

2.7. Surface Plasmon Resonance measurement of selected compounds

The most potent compounds were assessed for DYRK1A target engagement by Surface Plasmon Resonance (SPR) to measure the binding constants and association and dissociation rates (Table 9). The measured K_D values of compounds **17**, **21** and **29** were in good agreement with the data from the TR-FRET based binding displacement assay. All compounds showed fast binding kinetics, with similar off-rates.

2.8. Metabolic stability and solubility of selected compounds

Several analogues had emerged with superior DYRK1A binding affinity compared to the original starting point, fragment **1** (LE = 0.52, LLE = 4.11 and pIC_{50} = 5.58). Aiming to identify a compound suitable for *in vivo* studies, analogues were profiled for solubility and metabolic stability in-house. Incorporation of the lipophilic 3-(trifluoromethoxy) phenyl motif (compounds **17** and **21**) led to increased turnover in human microsomes and a significant reduction in aqueous solubility. Replacement of the 3-(trifluoromethoxy)phenyl substituent with an unsaturated tetrahydropyran moiety (compound **27**), resulted in improved solubility and increased stability in human microsomes, suggesting that the 3-position of the imidazo [1,2-*b*]pyridazine scaffold can be optimized to modulate *in vitro* ADME properties without being detrimental to DYRK1A binding affinity. Some compounds designed specifically to increase polarity and/or Fsp^3 [47] did exhibit superior aqueous solubility (compounds **25** and **27**), whilst others did not (compound **24** and **26**). All compounds were rapidly cleared in rat liver microsomes so were not suitable for progression to a rat IV PK study or *in*

Fig. 4. NanoBRET analysis of the direct binding of compound **17** to DYRK1A in HEK293 cells. Two biological replicates were made at different tracer concentrations, plotted separately on the graph. The IC_{50} values were 50 nM in the presence of 2 μM tracer and 41 nM in the presence of 1 μM tracer.

Table 9
Surface Plasmon Resonance Measurement binding kinetics and affinity of selected compounds.

Compound	k_a ($M^{-1}s^{-1}$)	k_d (s^{-1})	K_D (nM)
17	5.2 (±0.1) x 10^5	0.01 ± 0.01	22.5 ± 0.01
21	1.0 (±0.1) x 10^6	0.02 ± 0.01	21 ± 9
29	2.5 (±0.1) x 10^5	0.01 ± 0.01	31.4 ± 0.02

vivo model of disease (Table 10).

3. Conclusion

Starting from a ligand-efficient imidazo [1,2-*b*]pyridazine fragment **1**, we have identified and optimized a series of DYRK1A inhibitors. SAR investigation of aryl and heteroaryl groups at the C-6 position led us to discover that the 4-pyridyl motif was key to DYRK1A inhibition. Flanking the 4-pyridyl with a methyl or methoxy group was well

Table 10
Metabolic stability and solubility of selected compounds.

Compound	DYRK1A IC_{50}	HLM (μg/(min mg))	RLM (μg/(min mg))	Solubility (μM)
1	2640	12 ± 2	114 ± 1	>250
4	419	28 ± 1	107 ± 7	>250
17	25	173 ± 21	104 ± 15	<0.5
21	96	71 ± 3	129 ± 4	2
24	180	N.T.	N.T.	2
25	1450	N.T.	N.T.	73
26	579	N.T.	N.T.	4
27	123	62 ± 2	114 ± 3	72

[a] IC_{50} (nM) in TR-FRET-based ligand-binding displacement assay measured with two technical replicates (n = 1 biological replicate). LE = 1.4(pIC_{50})/n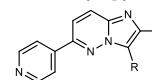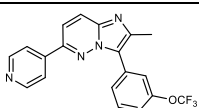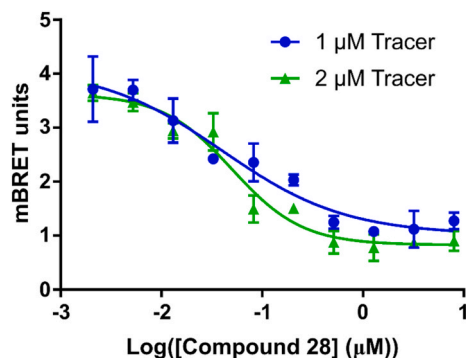on-hydrogen atoms. LLE = pIC_{50} – clog P. HLM and RLM determinations mean of n = 2 ± standard deviation (unless otherwise stated). HLM = human liver microsomes, RLM = rat liver microsomes; thermodynamic solubility data was derived from a single experiment at pH 6.8. N.T. = Not tested due to lower DYRK1A IC_{50} (nM).

Table 8
Selectivity of chimeric compound **29**.

Compound	Structure	DYRK1A	CLK1	CLK2	Haspin
29		19.6	>10000	17.5	39.3

[a]Kd (nM) in BLI assay measured with two technical replicates (n = 1 biological replicate).

tolerated and has the potential to improve kinome selectivity. Installation of the 3-(trifluoromethoxy)phenyl substituent at the C-3 position, directed beneath the P-loop, increased DYRK1A potency significantly, resulting in compound **17**, a potent cellular DYRK1A inhibitor with good selectivity over the kinome (S-score (35) = 0.136). The addition of a methyl group to the C-2 position to give compound **29**, increased the selectivity of the series with respect to mutagenic CLK kinases off-targets. Significant liabilities for the series were found to be low aqueous solubility and rapid *in vitro* metabolism. In terms of compound quality, compounds had high lipophilicity (logP >3) and high aromatic ring count (4). Current efforts are focused on improving the solubility and metabolic stability of the imidazo [1,2-*b*]pyridazine series, specifically by more focused exploration of the 3-position of the imidazo [1,2-*b*]pyridazine core, with an emphasis on lowering lipophilicity and the number of aromatic rings to reduce the potential for π-stacking. In parallel, efforts are underway to translate the established SAR of the imidazo [1,2-*b*]pyridazine series to the intrinsically more potent and less lipophilic imidazo [1,2-*a*]pyridine and imidazo [1,2-*a*]pyrimidine cores, with the aim of furnishing a compound suitable for use in disease-relevant *in vivo* models associated with DYRK1A overexpression.

4. Materials and Methods

4.1. Cloning

For expression of protein for crystallisation a plasmid containing DNA for residues 127–485 of human DYRK1A isoform 1 (NCBI reference NP_001387) with an N-terminal hexahistidine tag for purification was used as previously described [1]. For expression of protein for binding-displacement assays DNA for DYRK1A residues 127–485 was cloned into expression plasmid pNIC-Bio 3 which expressed the desired region of DYRK1A fused to an N-terminal tobacco etch virus (TEV) protease cleavable hexahistidine tag (extension MHHHHHHSSGVDLGTENLYFQ*SM where * represents the position of digestion by TEV protease) and a C-terminal avidin tag (extension SSSKGGYGLNDIFEAQKIEWHE).

4.2. DYRK1A protein expression and purification

The DYRK1A constructs were transformed into *Escherichia coli* strain BL21 (DE3)-R3 also with a plasmid expressing the bacteriophage lambda phosphatase and three rare tRNAs resulting in protein that is mono-phosphorylated on residue Y321. For binding-displacement assay the construct was co-expressed with birA to produce the biotinylated protein. The resulting colonies were used to inoculate LB medium (Miller) containing 50 μg/mL kanamycin and 34 μg/mL chloramphenicol and cells allowed to grow overnight with shaking at 200 rpm, 37 °C. The following morning, 10 mL of this culture was used to inoculate each 1 L volume of TB media containing 50 μg/mL kanamycin. The cultures were grown at 37 °C with shaking until an OD_{600} of 1.4 was reached, then the temperature was reduced to 18 °C. At an OD_{600} of 1.6, isopropyl β-D-1-thiogalactopyranoside (IPTG) was added to a final concentration of 0.4 mM to induce expression overnight, along with 0.3 mM biotin for production of the biotinylated protein. Cells were harvested by centrifugation and then re-suspended in 25 mL of Binding Buffer (50 mM HEPES pH 7.5, 500 mM NaCl, 5 mM imidazole, 5% glycerol, 0.5 mM tris(2-carboxyethyl)phosphine (TCEP) per litre of culture, and stored frozen at −20 °C until required.

Thawed cells were lysed by sonication and polyethylenimine (PEI) was added to a final concentration of 0.15% prior to centrifugation to remove insoluble material. The supernatant was passed through a column of 2.5 mL Ni-Sepharose resin (GE Healthcare). The resin was washed with Binding Buffer containing increasing amounts of imidazole before elution with Binding Buffer containing 250 mM imidazole. The eluate was incubated at 4 °C overnight with TEV protease to remove the purification tag, then concentrated to 5 mL and injected on a S75 16/60

gel filtration column (GE Healthcare) pre-equilibrated into GF Buffer (50 mM HEPES pH 7.5, 300 mM NaCl, 5% glycerol, 0.5 mM TCEP). Purified proteins were concentrated using 30 kDa MWCO centrifugal filters devices (Millipore) at 4 °C prior to flash freezing, aliquoting and storage at −80 °C. Protein concentrations were measured by UV absorbance using a NanoDrop spectrophotometer (Thermo Scientific) and the calculated molecular weights and estimated extinction co-efficients based on the protein amino acid sequence. Protein identities were confirmed by electrospray ionization mass spectrometry (ESI-MS).

4.3. Crystallisation, data collection, and processing

For crystallisation, DYRK1A at a concentration of ~15 mg/mL was thawed rapidly and incubated with 0.5–1.5 mM inhibitor (from a stock solution in 100% DMSO) on ice for 15 min, limiting the final DMSO concentration in the solution to <5%. The solution was centrifuged at 21,000×g for 15 min at 4 °C to remove any precipitated compound material prior to setting up crystallisation plates. Crystals were obtained using the sitting drop vapour diffusion method at 4 °C in various conditions (listed in Table 1) from total drop volumes of 150 nL and ratios of protein to well solution of 2:1, 1:1 or 1:2, equilibrated against 20 μL of reservoir solution. Crystals typically grew in less than 14 days and were cryo-protected by direct addition of 1 μL reservoir solution spiked with 25% ethylene glycol to the crystallisation drop, then immediately harvested and flash frozen in liquid nitrogen for storage.

All data was collected at 100 K at the Diamond Synchrotron. Data collection statistics can be found in Table 1. The diffraction data was indexed and integrated using MOSFLM [2] or XDS [3], and scaled using AIMLESS [4] and structures solved by molecular replacement using PHASER [5] with a previous structure of human DYRK1A as a search model. The models were built using several rounds of manual and automated refinement using Coot [6] and REFMAC5 [7] or Phenix [8] prior to modelling of the ligand into the corresponding electron density. Ligand restraints were generated using the Grade web server [9]. All models were validated using MolProbity [10] prior to deposition in the PDB under the deposition IDs listed in Table 1.

4.4. TR-FRET binding assay

The method assesses the ability of inhibitors to displace a fluorescent tracer molecule from the ATP-binding site of a kinase protein tagged with a FRET donor. If the tracer molecule is displaced, the FRET signal is lost. Inhibitors were dissolved in DMSO and dispensed as 16-point, 2x serial dilutions in duplicate into black multi-well plates (Greiner). Each well contained 2 nM biotinylated DYRK1A kinase domain ligated to streptavidin-Tb-cryptate (Cisbio), 25 nM Kinase Tracer 236 (Thermo-Fisher Scientific), 10 mM Hepes pH 7.5, 150 mM NaCl, 2 mM DTT, 0.01% BSA, 0.01% Tween-20. Final assay volume for each data point was 5 μL, and final DMSO concentration was 1%. After setting up the assay plate it was incubated at room temperature for 1.5 h and then read using a TR-FRET protocol on a PheraStarFS plate reader (BMG Labtech). The data was normalized to 0% and 100% inhibition control values and fitted to a four parameter dose-response binding curve in GraphPad Software (version 7, La Jolla, CA, USA). The determined IC_{50} values were converted to K_i values using the Cheng-Prusoff equation and the concentration and K_D values for the tracer (previously determined).

4.5. Radiometric kinase assay

The radiometric kinase assay (^{33}PanQinase® Activity Assay) was provided by Proqinase GmbH.: The assay was used for measuring the kinase activity of DYRK1A, CDK2 and GSK3β protein kinase in the presence and absence of test compound. In a ScintiPlate microtiter plate: Transfer 20 μL buffer; add 5 μL 10% DMSO (with or without test compound); add 10 μL substrate (in 50 mM HEPES pH 7.5); add 10 μL recombinant protein kinase; add 5 μL ATP (in H_2O); mix on shaker;

incubate for 60 min at 30 °C; stop the reaction with 50 μL 2% H_3PO_4; mix on shaker; wash 3 times with 200 μL 0.9 % NaCl; count dry plate with a scintillation counter. The reaction takes place in ScintiPlate-96 (Cat. # 6005349, PerkinElmer), which are coated with a scintillant. Proteins and peptides bind to the surface of the plates, which allows us to use natural substrates in our assays. No artificial modification of the substrates is necessary. The assay contained 60 mM HEPES-NaOH, pH 7.5, 3 mM $MgCl_2$, 3 mM $MnCl_2$, 3 μM Na-orthovanadate, 1.2 mM DTT, 50 μg/ml PEG20000, 1 μM [gamma-33 P]-ATP (approx. 3×105 cpm per well), protein kinase, and substrate.

4.6. Thermal shift assay

An in-house kinase panel was set up to cover representative members of each major family. Proteins were expressed in E. coli or insect cells, purified to 95% purity or better after tag removal. Fluorescence-based thermal shift assays were set up in 384-well plates using 20 μL sample volumes containing 1 μM enzymes dissolved in buffer 100 mM K2HPO4 pH7.5 containing 1x dye (Applied Biosystems, 4461146). Compounds dissolved in DMSO to 10 mM were added using an automated liquid dispensing unit (Felix CyBio) fitted with a robotic pin tool (V&P scientific) capable of transferring 20 nL of each compound to the assay plate to a final concentration of 10 μM. Melting curves were generated in an Applied Biosystems (now Thermo Fisher Scientific) QuantStudio 6 qPCR equipment, set to ramp from 25 to 95 °C at a rate of 0.05 °C/s. Data were processed with Protein Thermal Shift Software version 1.3 using a Boltzmann function fit to calculate melting temperatures (Tm B) and differential melting temperatures (deltaTm B) with protein in 0.1% DMSO as reference. Staurosporine was used as a broad-spectrum positive control at 10 μM. Data was generated once with no repetition.

Kinases used in the in-house panel: AAK1, BMP2K, BMXA, BRAFA, CAMK1D, CAMK1G, CAMKK1, CAMKK2B, CDC42BPA,CDK2, CDKL1, CHEK2, CLK1, CSNK1G1, CSNK1G3, CSNK2A1, DYRK1AA, DYRK2A, EPHA2A, GAKA, GSG2A, MAPK1A, MAP2K7A, MAPK14B, MAPK3A, PHKG2A, PIM1A, PLK1A, PKMYT1A, PRPF4BA, RPS6KA1A, RPS6KA5A, RPS6KA6A, SLKA, SRPK1A, SRPK2A, STK3, STK6A, STK10A, STK17AA, STK24A, STK38LA, TRIB2A, TTKA, VRK1, VRK2A.

4.7. Biolayer interferometry (BLI) CMGC panel assay

Biolayer Interferometry (BLI) is an optical technique that measures macromolecular interactions by analyzing interference patterns of white light reflected from the surface of a biosensor tip. A CMGC kinase panel experiment was ran using biotinylated kinases (DYRK1A, CLK1, CLK2, Haspin) immobilised onto super-streptavidin biosensors and dipped into wells containing test compound. Concentration-response experiments were ran from 10 μM to 5 nM in 3 x dilution series (8 points) for each compound (2% DMSO final concentration in assay buffer) against each protein, and subtracted the signal from the reference sensors (no protein immobilised). The overall response values against compound concentration were plotted in GraphPad and fit with nonlinear "One site – total" binding model to obtain the KD values.

4.8. NanoBRET kinase assay

Compounds were tested for direct binding to DYRK1A in live cells using a nanoluciferase (nanoLuc) bioluminescence resonance energy transfer (BRET) (NanoBRET, Promega) target engagement assay established in-house. The NanoBRET assay measured the ability of a compound to displace a fluorescent tracer molecule from the ATP-binding site of DYRK1A protein N-terminally fused with NanoLuc luciferase (Nluc) in HEK293 cells. In the absence of test compound, the fusion protein and tracer molecule were in proximity and able to generate a detectable BRET signal.

NanoLuc/target fusion constructs were complexed with Lipofectamine 2000 according to the manufacturer's protocol (Invitrogen).

DNA:Lipofectamine complexes were formed at a ratio of 2:5 (μg DNA per μl FuGENE). The transfection complexes were then mixed with HEK293t cells (ATCC) in a 100 mm dish at 95% confluence in serum-free DMEM (Lonza), followed by incubation in a humidified, 37 °C/5% CO_2 incubator for 20 h. Cells were trypsinized and resuspended in Opti-MEM without phenol red (Life Technologies). Cells (85 μL) were then seeded into white, nonbinding surface plates (Corning) at a density of 2 $\times 10^5$ cells/mL. Diluted tracer was prepared from 200 μM stock in Tracer Diluted Buffer (32,25% PEG400 in 12.5 mM HEPES Buffer pH7.5) at 1 to 4 ratio, and 10 μL was added to the cells to have a final concentration of 2, 1, 0.5 or 0.25 μM. All chemical inhibitors were prepared as concentrated stock solutions in dimethylsulphoxide (DMSO) (Sigma-Aldrich). Cells were then incubated for 2 h before BRET measurements. To measure BRET, NanoBRET NanoGlo Substrate-(Promega) was added, and filtered luminescence was measure on a BMG LABTECH Clariostar luminometer equipped with 450 nm BP filter (donor) and 610 nm LP filter (acceptor), using 0.5 s integration time with gain settings of 3600 and 3,600, respectively. Background-corrected BRET ratios were determined by subtracting the BRET ratios of samples with no tracer added. All data points were measured in triplicate with blank wells (no tracer), wells with DMSO only (vehicle) as negative control and staurosporine as positive control. Controls were measured in sextuplicate.

4.9. Surface plasmon resonance measurements

Biacore T200 (GE healthcare) and SPR 32 (Bruker) instruments were used to screen the compounds for binding to DYRK1A protein. DYRK1A was captured via Biotin tag on neutravidin or streptavidin surface of a SPR 32 or Biacore T200 biosensor chip respectively. To minimise mass transport of the compound/protein interaction capture level was kept at below 1000 RU. Compounds were screened at a flow rate 100 μL/min. Association was measured for 60 s and dissociation for 60–300 s depending on the off-rate of each compound. Each compound was screened at 6–8 concentrations in a 3-fold dilution concentration series. The top concentration was adjusted according to binding affinity to 10 or 5 μM. Running buffer contained 50 mM Tris·HCl (pH 7.4), 150 mM NaCl, 10 mM $MgCl_2$, 0.05% Tween 20, 3% DMSO. Data were analysed using Scrubber 2 (BioLogic software, Australia). All sensorgrams were corrected using DMSO calibration and double referenced for blank injection of buffer and reference surface. Data were fitted to a 1:1 binding model including mass transport coefficient.

5. DiscoverX KinomeSCAN selectivity assay

For whole kinome selectivity profiling, inhibitors were profiled against the kinase panel of DiscoverX Corporation (California, USA) at a concentration of 1.0 μM, as previously described [11].

All References for Materials and Methods are found in the Supporting information.

6. Synthetic chemistry protocols for key compounds

All commercial reagents were purchased from Sigma-Aldrich, Alfa Aesar, Apollo Scientific, Fluorochem or Tokyo Chemical Industry and of the highest available purity. Unless otherwise stated, chemicals were used as supplied without further purification. Anhydrous solvents were purchased from Acros (AcroSeal™) or Sigma-Aldrich (SureSeal™) and were stored under nitrogen. Anhydrous solvents and reagents were used as purchased. Thin layer chromatography (TLC) was carried out using glass plates pre-coated with Merck silica gel 60 F254. Melting point measurements are recorded on MPA100 OptiMelt apparatus and are uncorrected. Proton nuclear magnetic resonance spectra were recorded at 500 MHz on a Varian VNMRS 500 MHz spectrometer or at 600 MHz on a Varian VNMRS 600 MHz spectrometer or at 500 MHz on a Bruker Biospin GmbH 500 MHz spectrometer, using residual isotopic solvent (CHCl$_3$, δ_H = 7.27 ppm, DMSO δ_H = 2.50 ppm, MeOH δ_H = 3.31 ppm,

DMF δ_H = 2.92) as an internal reference. Chemical shifts are quoted in parts per million (ppm). Coupling constants (J) are recorded in Hertz (Hz). Carbon nuclear magnetic resonance spectra were recorded at 125 MHz on a Varian 500 MHz spectrometer or 151 MHz on a Varian 600 MHz spectrometer, using residual isotopic solvent (CHCl$_3$, δ_C = 77.00 ppm, DMSO δ_C = 39.52 ppm, MeOH δ_C = 49.00 ppm) as an internal reference. Proton and carbon spectra assignments are supported by DEPT editing. Chemical shifts (δ_C) are quoted in ppm. Low resolution mass spectrometry data (EI) were recorded on Fission Instrument VG autospec at 70eV. High resolution mass spectrometry data (ESI) were recorded on Bruker Daltonics, Apex III, ESI source: Apollo ESI with methanol as spray solvent. Only molecular ions, fractions from molecular ions and other major peaks are reported as mass/charge (m/z) ratios. LCMS-LCQ data was recorded on a Waters 2695 HPLC using a Waters 2487 UV detector and a Thermo LCQ ESI-MS. Samples were eluted through a Phenomenex Lunar 3 μm C18 50 mm × 4.6 mm column, using water and acetonitrile acidified by 0.1% formic acid at 1 ml/min and detected at 254 nm. The gradient employed was a 4 min method 10–90% MeCN over a 4 min gradient, held at 90% MeCN for 1 min, then re-equilibrated over 1 min. LCMS-MDAP analytical data was recorded on a Shimadzu Prominence Series coupled to a LCMS-2020 ESi and APCI mass spectrometer. Samples were eluted through a Phenomenex Gemini 5μ C18 110A 250 mm × 4.6 mm column, using water and acetonitrile acidified by 0.1% formic acid at 1 ml/min and detected at 254 nm. The gradient employed was a 30 min method 5–95% MeCN over a 20 min gradient, held at 95% MeCN for 4 min, then re-equilibrated to 30% MeCN over 5 min.

6.1. 6-(4-Pyridyl)imidazo [1,2-b]pyridazine 1

To a sealed and degassed microwave vial containing 6-chloroimidazo [1,2-*b*]pyridazine (1.00 g, 6.51 mmol), pyridine-4-boronic acid hydrate (1.20 g, 9.77 mmol), bis [2-(di-*tert*-butylphosphanyl)cyclopenta-2,4-dien-1-yl]iron; dichloropalladium (50.0 mg, 0.08 mmol), and sodium carbonate (1.38 g, 13.02 mmol) was added acetonitrile (10 mL) and water (0.5 mL) and the reaction mixture was heated to 80 °C overnight. The reaction mixture was concentrated under reduced pressure. The residue was partitioned between EtOAc (50 mL) and water (50 mL) and the aqueous layer removed. The aqueous layer was extracted with EtOAc (50 mL x 3). The organic components were combined and washed with brine solution (100 mL), dried over MgSO$_4$, filtered and concentrated under reduced pressure. The crude was purified using flash silica column chromatography on an Isco Combiflash system (12 g silica, elution with 0–50% 20% MeOH in CH$_2$Cl$_2$/CH$_2$Cl$_2$ gradient). Desired fractions were concentrated under reduced pressure to afford the title compound, 6-(4-pyridyl)imidazo [1,2-*b*]pyridazine, **1**, as an off-white solid (400 mg, 1.94 mmol, 30.0% yield). R_f 0.66 (MeOH/CH$_2$Cl$_2$ 1:9); m. p. 146–148 °C; $\bar{\nu}_{max}$ (neat)/cm^{-1} 3132(C-H, w), 3091(C-H, w), 3076 (C-H, w), 1603 (C=N, m), 1557 (C=C, m), 1537 (C=C, m); ^{1}H NMR (500 MHz, DMSO-d_6) δ 8.75–8.70 (m, 2H), 8.38 (s, 1H), 8.27 (d, J = 9.5 Hz, 1H), 8.03–7.98 (m, 2H), 7.86 (d, J = 9.6 Hz, 1H), 7.84 (s, 1H); ^{13}C NMR (126 MHz, DMSO-d_6) δ 150.56, 149.02, 142.21, 138.08, 134.86, 126.27, 121.03, 117.48, 115.93; HRMS m/z (ESI$^+$) [Found: 197.0819, C$_{11}$H$_9$N$_4$ requires [M + H]$^+$ 197.0822]; LCMS (LCQ): Rt = 0.6 min; m/z (ESI$^+$) 197.3 [M + H]$^+$; LCMS (MDAP): Rt = 7.5 min; m/z (ESI$^+$) 197.1 [M + H]$^+$. Literature compound: Current Patent Assignee: ARIZONA BOARD OF REGENTS - US2020/39989, 2020, A1.

6.2. 6-Chloro-3-[3-(trifluoromethoxy)phenyl]imidazo [1,2-b]pyridazine I-5

To a sealed and degassed microwave vial containing 3-bromo-6-chloroimidazo [1,2-*b*]pyridazine (250 mg, 1.08 mmol), [3-(trifluoromethoxy)phenyl]boronic acid (220 mg, 1.08 mmol), cesium carbonate (700 mg, 2.15 mmol) and [1,1′-bis(diphenylphosphino) ferrocene]dichloropalladium (II) (4.00 mg, 0.05 mmol) was added water (0.5 mL) and 1,4-dioxane (3 mL). The reaction mixture was heated to 110 °C for 16 h. The reaction mixture was concentrated under reduced pressure. The residue was purified using flash silica column chromatography on an Isco Combiflash system (12 g silica, elution with 15% EtOAc/petroleum ether gradient). Recrystallisation in petroleum ether afforded the title compound, 6-chloro-3-[3-(trifluoromethoxy) phenyl]imidazo [1,2-*b*]pyridazine, **I-5**, as a pale yellow solid (200 mg, 0.61 mmol, 56.0% yield). R_f 0.55 (EtOAc/petroleum ether 1:1); m. p. 71–73 °C; $\bar{\nu}_{max}$ (neat)/cm^{-1} 3055 (C-H, m), 3030 (C-H, m), 1610 (C=N, m), 1514 (C=C, m); 1132 (C-O, s); ^{1}H NMR (500 MHz, DMSO-d_6) δ 8.49 (s, 1H), 8.37 (d, J = 9.5 Hz, 1H), 8.21 (s, 1H), 8.18 (d, J = 7.9 Hz, 1H), 7.72 (t, J = 8.1 Hz, 1H), 7.51 (d, J = 9.4 Hz, 1H), 7.47–7.43 (m, 1H); ^{13}C NMR (126 MHz, DMSO-d_6) δ 148.59, 146.38, 138.95, 134.42, 130.63, 129.80, 128.07, 125.99, 124.86, 120.16 (q, J = 256.6 Hz, 120.05, 118.95, 118.06; HRMS m/z (ESI$^+$) [Found: 314.0311., C$_{13}$H$_7$ClF$_3$N$_3$O requires [M + H]$^+$ 314.0303]; LCMS (LCQ): Rt = 4.8 min; m/z (ESI$^+$) 314.3 [M + H]$^+$; LCMS (MDAP): Rt = 18.4 min; m/z (ESI$^+$) 314.0 [M + H]$^+$; The spectroscopic data are in good agreement with the literature values Literature reference: US2009093475A1

6.3. 6-(4-Pyridyl)-3-[3-(trifluoromethoxy)phenyl]imidazo [1,2-b] pyridazine 17

To a sealed and degassed microwave vial containing 6-chloro-3-[3-(trifluoromethoxy)phenyl]imidazo [1,2-*b*]pyridazine (40.0 mg, 0.13 mmol), pyridine-4-boronic acid hydrate (16.0 mg, 0.13 mmol), sodium carbonate (27.0 mg, 0.26 mmol) and bis(triphenylphosphine)palladium (II) dichloride (5.00 mg, 0.01 mmol) was added water (0.10 mL) and acetonitrile (0.50 mL). The reaction mixture was irradiated with microwaves for 15 min at 150 °C. The reaction mixture was concentrated under reduced pressure. The residue was partitioned between EtOAc (30 mL) and water (30 mL), and extracted. The organic components were washed with water (2 x 30 mL), saturated brine solution (1 x 30 mL), and finally sodium hydroxide (2 x 30 mL). The combined organic components were dried over MgSO$_4$, filtered and concentrated to dryness under reduced pressure. The residue was purified using flash silica column chromatography on an Isco Combiflash system (12 g silica, elution with 0–50% 20% MeOH in CH$_2$Cl$_2$/CH$_2$Cl$_2$ gradient) to afford the title compound, 6-(4-pyridyl)-3-[3-(trifluoromethoxy)phenyl]imidazo [1,2-*b*]pyridazine, **17**, as a yellow solid (25.0 mg, 0.07 mmol, 55.0% yield). R_f 0.41 (MeOH/CH$_2$Cl$_2$ 1:9); m. p. 166–168 °C; $\bar{\nu}_{max}$ (neat)/cm^{-1} 2975 (C-H, m), 2918 (C-H, m), 1615 (C=N, m), 1478 (C=C, m), 1152 (C-O, s); ^{1}H NMR (500 MHz, DMSO-d_6) δ 8.83–8.79 (m, 2H), 8.50 (s, 1H), 8.43 (d, J = 9.5 Hz, 1H), 8.37 (s, 1H), 8.26 (dd, J = 8.1, 1.4 Hz, 1H), 8.12–8.09 (m, 2H), 8.03 (d, J = 9.5 Hz, 1H), 7.72 (t, J = 8.0 Hz, 1H), 7.43 (d, J = 8.0 Hz, 1H); ^{13}C NMR (151 MHz, DMSO-d_6) δ 150.56, 149.15, 148.69, 142.29, 139.90, 134.99, 130.90, 130.39, 126.87, 126.12, 125.24, 121.04, 120.50 (q, J = 240.6 Hz), 120.23, 118.22, 116.13; HRMS m/z (ESI$^+$) [Found: 357.0959., C$_{18}$H$_{11}$F$_3$N$_4$O requires [M + H]$^+$ 357.0958]; LCMS (LCQ): Rt = 3.4 min; m/z (ESI$^+$) 357.3 [M + H]$^+$; LCMS (MDAP): Rt = 13.8 min; m/z (ESI$^+$) 357.0 [M + H]$^+$.

6.4. 6-Chloro-2-methyl-imidazo [1,2-b]pyridazine I-2

To a microwave vial containing 6-chloropyridazin-3-amine (2.35 g, 36.7 mmol) in EtOH (15 mL) was added chloroacetone (3.39 g, 36.7 mmol) and TEA (2.53 mL). The reaction mixture was heated to 150 °C and stirred for 1 h. The reaction mixture was concentrated under reduced pressure. The crude was purified using flash silica column chromatography on an Isco Combiflash system (40 g silica, elution with 30–50% EtOAc/petroleum ether gradient). Desired fractions were combined and concentrated under reduced pressure to afford 6-chloro-2-methyl-imidazo [1,2-*b*]pyridazine, **I-2**, as an off-white solid (2.80 g, 15.9 mmol, 87.0% yield). R_f 0.65 (MeOH/CH$_2$Cl$_2$ 1:9); ^{1}H NMR (500 MHz, DMSO-d_6) δ 8.10 (s, 1H), 8.07 (d, J = 9.5 Hz, 1H), 7.28 (d, J = 9.4 Hz, 1H), 2.37 (s, 3H).; LCMS (LCQ): Rt = 0.9 min; m/z (ESI$^+$) 168.2 [M +

H]$^+$; LCMS (MDAP): Rt = 10.8 min; m/z (ESI$^+$) 168.1 [M + H]$^+$.

6.5. 2-Methyl-6-(4-pyridyl)imidazo [1,2-b]pyridazine 4

To a sealed and degassed vial containing pyridine-4-boronic acid hydrate (220 mg, 1.79 mmol), bis [2-(di-*tert*-butylphosphanyl)cyclopenta-2,4-dien-1-yl]iron; dichloropalladium (29.0 mg, 0.04 mmol), sodium carbonate (190 mg, 1.79 mmol), and 6-chloro-2-methyl-imidazo [1,2-*b*]pyridazine (150 mg, 0.89 mmol) was added acetonitrile (2.0 mL) and water (0.2 mL). The reaction mixture was heated to 80 °C and stirred overnight. Additional equivalents of pyridine-4-boronic acid hydrate (220 mg, 1.79 mmol), sodium carbonate (190 mg, 1.79 mmol) and bis [2-(di-*tert*-butylphosphanyl)cyclopenta-2,4-dien-1-yl]iron; dichloropalladium (29.0 mg, 0.04 mmol) were added, the vial was degassed, and the reaction was irradiated with microwaves at 140 °C for 25 min. The reaction mixture was concentrated under reduced pressure. The residue was partitioned between EtOAc (30 mL) and water (30 mL), and the organic layers separated. The aqueous layer was extracted with EtOAc (2 x 30 mL). The organic components were combined, washed with brine solution (50 mL), dried over MgSO$_4$, filtered and concentrated under reduced pressure. The crude was purified using flash silica column chromatography on an Isco Combiflash system (12 g silica, elution with 0–50% 20% MeOH in CH$_2$Cl$_2$/CH$_2$Cl$_2$ gradient). Desired fractions were combined and concentrated under reduced pressure to afford 2-methyl-6-(4-pyridyl)imidazo [1,2-*b*]pyridazine, **4**, as a pale yellow solid. (140 mg, 0.63 mmol, 71.0% yield). R$_f$ 0.45 (MeOH/CH$_2$Cl$_2$ 1:9); m. p. 84–86 °C; $\bar{v}_{max}$ (neat)/cm^{-1} 3131 (C-H, w), 3040(C-H, w), 2927 (C-H, w), 1599 (C=N, m), 1594 (C=C, m), 1546 (C=C, m); 1531 (C=C, m); ^{1}H NMR (500 MHz, DMSO-d_6) δ 8.75 (d, J = 4.5 Hz, 2H), 8.18 (s, 1H), 8.16 (d, J = 9.7 Hz, 1H), 8.02 (d, J = 4.5 Hz, 2H), 7.84 (d, J = 9.4 Hz, 1H), 2.42 (s, 3H); ^{13}C NMR (151 MHz, DMSO-d_6) δ 150.41, 147.86, 144.55, 142.24, 137.58, 124.75, 120.75, 115.00, 114.46, 14.59; HRMS m/z (ESI$^+$) [Found: 211.0988., C$_{12}$H$_{11}$N$_4$ requires [M + H]$^+$ 211.0978]; LCMS (LCQ): Rt = 0.5 min; m/z (ESI$^+$) 211.3 [M + H]$^+$; LCMS (MDAP): Rt = 8.0 min; m/z (ESI$^+$) 211.1 [M + H]$^+$.

6.6. 3-Bromo-2-methyl-6-(4-pyridyl)imidazo [1,2-b]pyridazine I-7

To a solution of 2-methyl-6-(4-pyridyl)imidazo [1,2-*b*]pyridazine (330 mg, 1.57 mmol) in DMF (3.0 mL) was added *N*-bromosuccinimide (300 mg, 1.69 mmol). The reaction mixture was stirred at rt overnight. The reaction mixture was concentrated under reduced pressure. The crude was purified using flash silica column chromatography on an Isco Combiflash system (24 g silica, elution with 0–50% 20% MeOH in CH$_2$Cl$_2$/CH$_2$Cl$_2$ gradient). Desired fractions were combined and concentrated under reduced pressure to afford **I-7** as a gold solid (600 mg, 1.04 mmol, 66.0% yield).

50 mg of the crude was purified using flash reverse phase column chromatography on a Biotage system (12 g C-18, elution with 10–100% MeOH/water gradient). Desired fractions were combined and concentrated under reduced pressure to afford 3-bromo-2-methyl-6-(4-pyridyl) imidazo [1,2-*b*]pyridazine, **I-7**, as a white solid (30.0 mg, 0.10 mmol). R$_f$ 0.43 (MeOH/CH$_2$Cl$_2$ 1:9); ^{1}H NMR (600 MHz, DMSO-d_6) δ 8.83–8.79 (m, 2H), 8.25 (d, J = 9.4 Hz, 1H), 8.13–8.07 (m, 2H), 7.97 (d, J = 9.5 Hz, 1H), 2.46 (s, 3H); LCMS (LCQ): Rt = 1.0 min; m/z (ESI$^+$) 289.2 [M]$^+$ and 291.2 [M+2]$^+$.

6.7. 2-Methyl-6-(4-pyridyl)-3-[3-(trifluoromethoxy)phenyl]imidazo [1,2-b]pyridazine 29

To a microwave vial containing bis [2-(di-*tert*-butylphosphanyl) cyclopenta-2,4-dien-1-yl]iron; dichloropalladium (23.0 mg, 0.03 mmol), [3-(trifluoromethoxy)phenyl]boronic acid (214 mg, 1.04 mmol), 3-bromo-2-methyl-6-(4-pyridyl)imidazo [1,2-*b*]pyridazine (200 mg, 0.35 mmol) and cesium carbonate (225 mg, 0.69 mmol) was added water (1 mL) and acetonitrile (8 mL). The reaction vial was evacuated

and backflushed with nitrogen x 3 before the reaction mixture was heated to 110 °C for 48 h. The reaction mixture was concentrated under reduced pressure. The crude was purified using flash silica column chromatography on an Isco Combiflash system (12 g silica, elution with 0–10% MeOH/EtOAc gradient). Desired fractions were combined and concentrated under reduced pressure. The residue was purified using flash reverse phase column chromatography on an Isco Combiflash system (20 g C-18, elution with 10–100% MeOH/water gradient). Desired fractions were combined and concentrated under reduced pressure. Desired fractions were combined and concentrated under reduced pressure to afford the desired product, 2-methyl-6-(4-pyridyl)-3-[3-(trifluoromethoxy)phenyl]imidazo [1,2-*b*]pyridazine, **29**, as a yellow solid (80.0 mg, 0.21 mmol, 59.0% yield). R$_f$ 0.37 (MeOH/CH$_2$Cl$_2$ 1:9); m. p. 126–128 °C; $\bar{v}_{max}$ (neat)/cm^{-1} 3095 (C-H, w), 3031 (C-H, w), 2923 (C-H, w), 1608 (C=N, m), 1597 (C=C, m), 1544 (C=C, m); 1212 (C-O, s), 1144 (C-O, s); ^{1}H NMR (600 MHz, cd$_3$od) δ 8.69 (d, J = 5.9 Hz, 2H), 8.13 (dd, J = 9.5, 0.9 Hz, 1H), 8.06–8.02 (m, 2H), 7.92 (dd, J = 9.5, 0.9 Hz, 1H), 7.86–7.77 (m, 2H), 7.69 (t, J = 8.0 Hz, 1H), 7.43–7.38 (m, 1H), 2.63 (s, 3H); ^{13}C NMR (151 MHz, cd$_3$od) δ 151.05, 150.56, 149.97, 145.01, 144.27, 139.40, 131.56, 131.46, 129.15, 125.95, 125.34, 122.81, 122.57, 121.99, 117.52, 14.84; HRMS m/z (ESI$^+$) [Found: 371.1113., C$_{19}$H$_{14}$F$_3$N$_4$O requires [M + H]$^+$ 371.1114]; LCMS (MDAP): Rt = 17.6 min; m/z (ESI$^+$) 371.9 [M + H]$^+$.

CRediT authorship contribution statement

Scott H. Henderson: Writing – review & editing, Writing – original draft, Methodology, Investigation, Data curation, Conceptualization. **Fiona J. Sorrell:** Investigation, Data curation, Conceptualization. **James M. Bennett:** Data curation. **Oleg Fedorov:** Conceptualization. **Marcus T. Hanley:** Data curation. **Paulo H. Godoi:** Data curation. **Roberta Ruela de Sousa:** Data curation. **Sean Robinson:** Data curation. **Iva Hopkins Navratilova:** Data curation. **Jonathan M. Elkins:** Writing – review & editing, Supervision, Conceptualization. **Simon E. Ward:** Writing – review & editing, Supervision, Investigation, Conceptualization.

Declaration of competing interest

The authors declare no financial competing interests.

Data availability

No data was used for the research described in the article.

Acknowledgements

Appendix A. Supplementary data

Supplementary data to this article can be found online at https://doi.org/10.1016/j.ejmech.2024.116292.

Abbreviations

BBB	blood-brain barrier
CDK	cyclin dependent kinase
CLK	CDC-like kinases
CMGC	Including cyclin-dependent kinases (CDKs), mitogen-activated protein kinases (MAP kinases), glycogen synthase kinases (GSK) and CDK-like kinases
CNS MPO	Central nervous system multi-parameter optimization
DYRK	Dual-specificity tyrosine phosphorylation-regulated kinase
GSK	Glycogen synthase kinases
HBA	hydrogen bond acceptor
HLM	human liver microsomes
LE	ligand efficiency
LLE	lipophilic ligand efficiency
MDCK-MDR1	Madin-Darby canine kidney cells transfected with the human MDR1 gene
MMP	matched-molecular pair
PDB	Protein databank
P-gp	permeability glycoprotein 1
PK	pharmacokinetics
RLM	rat liver microsomes
SAR	structure-activity relationship
SBDD	structure-based drug design

References

[1] R. Roskoski Jr., A historical overview of protein kinases and their targeted small molecule inhibitors, Pharmacol. Res. 100 (2015) 1–23, https://doi.org/10.1016/j.phrs.2015.07.010.

[2] J. Boni, C. Rubio-Perez, N. López-Bigas, C. Fillat, S. de la Luna, The DYRK family of kinases in cancer: molecular functions and therapeutic Opportunities, Cancers 12 (8) (2020) 2106, https://doi.org/10.3390/cancers12082106.

[3] V. Tandon, L. de la Vega, S. Banerjee, Emerging roles of DYRK2 in cancer, J. Biol. Chem. 296 (2021) 100233, https://doi.org/10.1074/jbc.REV120.015217.

[4] K. Yuan, H. Shen, M. Zheng, F. Xia, Q. Li, W. Chen, M. Ji, H. Yang, X. Zhuang, Z. Cai, W. Min, X. Wang, Y. Xiao, P. Yang, Discovery of potent DYRK2 inhibitors with high selectivity, great solubility, and excellent safety properties for the treatment of prostate cancer, J. Med. Chem. 66 (6) (2023) 4215–4230.

[5] O. Bogacheva, O. Bogachev, M. Menon, A. Dev, E. Houde, E.I. Valoret, H. M. Prosser, C.L. Creasy, S.J. Pickering, E. Grau, K. Rance, G.P. Livi, V. Karur, C. L. Erickson-Miller, D.M. Wojchowski, DYRK3 dual-specificity kinase attenuates erythropoiesis during anemia, J. Biol. Chem. 283 (52) (2008) 36665–36675, https://doi.org/10.1074/jbc.M807844200.

[6] C.L. Erickson-Miller, C. Creasy, A. Chadderton, C.B. Hopson, E.I. Valoret, M. Gorczyca, L. Elefante, D.M. Wojchowski, M. Chomo, D.M. Fitch, K.J. Duffy, GSK626616: a DYRK3 inhibitor as a potential new therapy for the treatment of anemia, Blood 110 (11) (2007) 510, https://doi.org/10.1182/blood.V110.11.510.510.

[7] J.G. Kettle, P. Ballard, C. Bardelle, M. Cockerill, N. Colclough, S.E. Critchlow, J. Debreczeni, G. Fairley, S. Fillery, M.A. Graham, L. Goodwin, S. Guichard, K. Hudson, R.A. Ward, D. Whittaker, Discovery and optimization of a novel series of Dyrk1B kinase inhibitors to explore a MEK resistance hypothesis, J. Med. Chem. 58 (6) (2015) 2834–2844, https://doi.org/10.1021/acs.jmedchem.5b00098.

[8] A. Szamborska-Gbur, E. Rutkowska, A. Dreas, M. Frid, M. Vilenchik, M. Milik, K. Brzózka, M. Król, How to design potent and selective DYRK1B inhibitors? Molecular modeling study, J. Mol. Model. 25 (2) (2019) 41, https://doi.org/10.1007/s00894-018-3921-3.

[9] R. Abbassi, T.G. Johns, M. Kassiou, L. Munoz, DYRK1A in neurodegeneration and cancer: molecular basis and clinical implications, Pharmacology & therapeutics 151 (2015) 87–98, https://doi.org/10.1016/j.pharmthera.2015.03.004.

[10] A. Ionescu, F. Dufrasne, M. Gelbcke, I. Jabin, R. Kiss, D. Lamoral-Theys, DYRK1A kinase inhibitors with emphasis on cancer, Mini reviews in medicinal chemistry 12 (13) (2012) 1315–1329, https://doi.org/10.2174/13895575112091315.

[11] E. Friedman, Mirk/Dyrk1B in cancer, J. Cell. Biochem. 102 (2) (2007) 274–279, https://doi.org/10.1002/jcb.21451.

[12] K. Kumar, C. Suebsuwong, P. Wang, A. Garcia-Ocana, A.F. Stewart, R.J. DeVita, DYRK1A inhibitors as potential therapeutics for β-cell regeneration for diabetes, J. Med. Chem. 64 (6) (2021) 2901–2922, https://doi.org/10.1021/acs.jmedchem.0c02050.

[13] E. Dirice, D. Walpita, A. Vetere, B.C. Meier, S. Kahraman, J. Hu, V. Dančík, S. M. Burns, T.J. Gilbert, D.E. Olson, P.A. Clemons, R.N. Kulkarni, B.K. Wagner, Inhibition of DYRK1A stimulates human β-cell proliferation, Diabetes 65 (6) (2016) 1660–1671, https://doi.org/10.2337/db15-1127.

[14] Wang, P., Alvarez-Perez, J. C., Felsenfeld, D. P., Liu, H., Sivendran, S., Bender, A., Kumar, A., Sanchez, R., Scott, D. K., Garcia-Ocaña, A., & Stewart, A. F., A high-throughput chemical screen reveals that harmine-mediated inhibition of DYRK1A increases human pancreatic beta cell replication. Nature medicine, 21(4), 383–388. https://doi.org/10.1038/nm.3820.

[15] P. Wang, E. Karakose, L. Choleva, K. Kumar, R.J. DeVita, A. Garcia-Ocaña, A. F. Stewart, Human beta cell regenerative drug therapy for diabetes: past achievements and future challenges, Front. Endocrinol. 12 (2021) 671946, https://doi.org/10.3389/fendo.2021.671946.

[16] V. Deshmukh, A.L. O'Green, C. Bossard, T. Seo, L. Lamangan, M. Ibanez, A. Ghias, C. Lai, L. Do, S. Cho, J. Cahiwat, K. Chiu, M. Pedraza, S. Anderson, R. Harris, L. Dellamary, S. Kc, C. Barroga, B. Melchior, B. Tam, Y. Yazici, Modulation of the Wnt pathway through inhibition of CLK2 and DYRK1A by lorecivivint as a novel, potentially disease-modifying approach for knee osteoarthritis treatment, Osteoarthritis Cartilage 27 (9) (2019) 1347–1360, https://doi.org/10.1016/j.joca.2019.05.006.

[17] T. Liu, Y. Wang, J. Wang, C. Ren, H. Chen, J. Zhang, DYRK1A inhibitors for disease therapy: Current status and perspectives, Eur. J. Med. Chem. 229 (2022) 114062, https://doi.org/10.1016/j.ejmech.2021.114062.

[18] D.B. Jarhad, K.K. Mashelkar, H.R. Kim, M. Noh, L.S. Jeong, Dual-specificity tyrosine phosphorylation-regulated kinase 1A (DYRK1A) inhibitors as potential therapeutics, J. Med. Chem. 61 (22) (2018) 9791–9810, https://doi.org/10.1021/acs.jmedchem.8b00185.

[19] B. Smith, F. Medda, V. Gokhale, T. Dunckley, C. Hulme, Recent advances in the design, synthesis, and biological evaluation of selective DYRK1A inhibitors: a new avenue for a disease modifying treatment of Alzheimer's? ACS Chem. Neurosci. 3 (11) (2012) 857–872, https://doi.org/10.1021/cn300094k.

[20] M.F. Lindberg, E. Deau, J. Arfwedson, N. George, P. George, P. Alfonso, A. Corrionero, L. Meijer, Comparative efficacy and selectivity of pharmacological inhibitors of DYRK and CLK protein kinases, J. Med. Chem. 66 (6) (2023) 4106–4130, https://doi.org/10.1021/acs.jmedchem.2c02068.

[21] M. Tarpley, H.O. Oladapo, D. Strepay, T.B. Caligan, L. Chdid, H. Shehata, J. R. Roques, R. Thomas, C.P. Laudeman, R.U. Onyenwoke, D.B. Darr, K.P. Williams, Identification of harmine and β-carboline analogs from a high-throughput screen of an approved drug collection; profiling as differential inhibitors of DYRK1A and monoamine oxidase A and for in vitro and in vivo anti-cancer studies, Eur. J. Pharmaceut. Sci. : official journal of the European Federation for Pharmaceutical Sciences 162 (2021) 105821, https://doi.org/10.1016/j.ejps.2021.105821.

[22] R. De la Torre, S. De Sola, M. Pons, A. Duchon, M.M. de Lagran, M. Farré, M. Fitó, B. Benejam, K. Langohr, J. Rodriguez, M. Pujadas, J.C. Bizot, A. Cuenca, N. Janel, S. Catuara, M.I. Covas, H. Blehaut, Y. Herault, J.M. Delabar, M. Dierssen, Epigallocatechin-3-gallate, a DYRK1A inhibitor, rescues cognitive deficits in Down syndrome mouse models and in humans, Mol. Nutr. Food Res. 58 (2) (2014) 278–288, https://doi.org/10.1002/mnfr.201300325.

[23] WO2017055530A1 (WIPO PCT).

[24] M.F. Lindberg, L. Meijer, Dual-specificity, tyrosine phosphorylation-regulated kinases (DYRKs) and cdc2-like kinases (CLKs) in human disease, an overview, Int. J. Mol. Sci. 22 (11) (2021) 6047, https://doi.org/10.3390/ijms22116047.

[25] C. Weber, M. Sipos, A. Paczal, B. Balint, V. Kun, N. Foloppe, P. Dokurno, A. J. Massey, D.L. Walmsley, R.E. Hubbard, J. Murray, K. Benwell, T. Edmonds, D. Demarles, A. Bruno, M. Burbridge, F. Cruzalegui, A. Kotschy, Structure-guided discovery of potent and selective DYRK1A inhibitors, J. Med. Chem. 64 (10) (2021) 6745–6764, https://doi.org/10.1021/acs.jmedchem.1c00023.

[26] D. Lee Walmsley, J.B. Murray, P. Dokurno, A.J. Massey, K. Benwell, A. Fiumana, N. Foloppe, S. Ray, J. Smith, A.E. Surgenor, T. Edmonds, D. Demarles, M. Burbridge, F. Cruzalegui, A. Kotschy, R.E. Hubbard, Fragment-derived selective inhibitors of dual-specificity kinases DYRK1A and DYRK1B, J. Med. Chem. 64 (13) (2021) 8971–8991, https://doi.org/10.1021/acs.jmedchem.1c00024.

[27] A.J. Massey, K. Benwell, M. Burbridge, A. Kotschy, D.L. Walmsley, Targeting DYRK1A/B kinases to modulate p21-cyclin D1-p27 signalling and induce anti-tumour activity in a model of human glioblastoma, J. Cell Mol. Med. 25 (22) (2021) 10650–10662, https://doi.org/10.1111/jcmm.17002.

[28] K. Kumar, P. Wang, J. Wilson, V. Zlatanic, C. Berrouet, S. Khamrui, C. Secor, E. A. Swartz, M. Lazarus, R. Sanchez, A.F. Stewart, A. Garcia-Ocana, R.J. DeVita, Synthesis and biological validation of a harmine-based, central nervous system (CNS)-Avoidant, selective, human β-cell regenerative dual-specificity tyrosine phosphorylation-regulated kinase A (DYRK1A) inhibitor, J. Med. Chem. 63 (6) (2020) 2986–3003, https://doi.org/10.1021/acs.jmedchem.9b01379.

[29] M. Sabha, B.C. Siaton, M.C. Hochberg, Lorecivivint, an intra-articular potential disease-modifying osteoarthritis drug, Expet Opin. Invest. Drugs 29 (12) (2020) 1339–1346, https://doi.org/10.1080/13543784.2020.1842357.

[30] Y. Yazici, T.E. McAlindon, A. Gibofsky, N.E. Lane, D. Clauw, M. Jones, J. Bergfeld, C.J. Swearingen, A. DiFrancesco, I. Simsek, J. Tambiah, M.C. Hochberg, Lorecivivint, a novel intraarticular CDC-like kinase 2 and dual-specificity tyrosine phosphorylation-regulated kinase 1A inhibitor and Wnt pathway modulator for the treatment of knee osteoarthritis: a phase II randomized trial, Arthritis Rheumatol. 72 (10) (2020) 1694–1706, https://doi.org/10.1002/art.41315.

[31] Y. Yazici, T.E. McAlindon, A. Gibofsky, N.E. Lane, C. Lattermann, N. Skrepnik, C. J. Swearingen, I. Simsek, H. Ghandehari, A. DiFrancesco, J. Gibbs, J.R.S. Tambiah, M.C. Hochberg, A Phase 2b randomized trial of lorecivivint, a novel intra-articular CLK2/DYRK1A inhibitor and Wnt pathway modulator for knee osteoarthritis, Osteoarthritis Cartilage 29 (5) (2021) 654–666, https://doi.org/10.1016/j. joca.2021.02.

[32] V. Deshmukh, M. Ibanez, H. Hu, J. Cahiwat, Y. Wei, J. Stewart, J. Hood, Y. Yazici, A small-molecule inhibitor of the Wnt pathway, lorecivivint (SM04690), as a potential disease-modifying agent for the treatment of degenerative disc disease, Spine J. : official journal of the North American Spine Society 20 (9) (2020) 1492–1502, https://doi.org/10.1016/j.spinee.2020.04.024.

[33] J.R.S. Tambiah, I. Simsek, C.J. Swearingen, S. Kennedy, B.J. Cole, T.E. McAlindon, Y. Yazici, Comparing patient-reported outcomes from sham and saline-based placebo injections for knee osteoarthritis: data from a randomized clinical trial of lorecivivint, Am. J. Sports Med. 50 (3) (2022) 630–636, https://doi.org/10.1177/03635465211067201.

[34] B. Melchior, G.K. Mittapalli, C. Lai, K. Duong-Polk, J. Stewart, B. Güner, B. Hofilena, A. Tjitro, S.D. Anderson, D.S. Herman, L. Dellamary, C.J. Swearingen, K.C. Sunil, Y. Yazici, Tau pathology reduction with SM07883, a novel, potent, and selective oral DYRK1A inhibitor: a potential therapeutic for Alzheimer's disease, Aging Cell 18 (5) (2019) e13000, https://doi.org/10.1111/acel.13000.

[35] B.Y. Tam, K. Chiu, H. Chung, C. Bossard, J.D. Nguyen, E. Creger, B.W. Eastman, C. C. Mak, M. Ibanez, A. Ghias, J. Cahiwat, L. Do, S. Cho, J. Nguyen, V. Deshmukh, J. Stewart, C.W. Chen, C. Barroga, L. Dellamary, S.K. Kc, Y. Yazici, The CLK inhibitor SM08502 induces anti-tumor activity and reduces Wnt pathway gene expression in gastrointestinal cancer models, Cancer letters 473 (2020) 186–197, https://doi.org/10.1016/j.canlet.2019.09.009.

[36] J. Kallen, C. Bergsdorf, B. Arnaud, M. Bernhard, M. Brichet, A. Cobos-Correa, A. Elhajouji, F. Freuler, I. Galimberti, C. Guibourdenche, S. Haenni, S. Holzinger, J. Hunziker, A. Izaac, M. Kaufmann, L. Leder, H.J. Martus, P. von Matt, V. Polyakov, P. Roethlisberger, A. Lerchner, X-Ray structures and feasibility assessment of CLK2 inhibitors for phelan-McDermid syndrome, ChemMedChem 13 (18) (2018) 1997–2007, https://doi.org/10.1002/cmdc.201800344.

[37] P. Grygier, K. Pustelny, J. Nowak, P. Golik, G.M. Popowicz, O. Plettenburg, G. Dubin, F. Menezes, A. Czarna, Silmitasertib (CX-4945), a clinically used CK2-kinase inhibitor with additional effects on GSK3β and DYRK1A kinases: a structural

perspective, J. Med. Chem. 66 (6) (2023) 4009–4024, https://doi.org/10.1021/acs.jmedchem.2c01887.

[38] I.H. Kaltheuner, K. Anand, J. Moecking, R. Düster, J. Wang, N.S. Gray, M. Geyer, Abemaciclib is a potent inhibitor of DYRK1A and HIP kinases involved in transcriptional regulation, Nat. Commun. 12 (1) (2021) 6607, https://doi.org/10.1038/s41467-021-26935-z.

[39] L.Z. Bendjeddou, N. Loaëc, B. Villiers, E. Prina, G.F. Späth, H. Galons, L. Meijer, N. Oumata, Exploration of the imidazo[1,2-b]pyridazine scaffold as a protein kinase inhibitor, Eur. J. Med. Chem. 125 (2017) 696–709, https://doi.org/10.1016/j.ejmech.2016.09.064.

[40] WO2020069418A1 (WIPO PCT).

[41] B. Wang, H. Wu, C. Hu, H. Wang, J. Liu, W. Wang, Q. Liu, An overview of kinase downregulators and recent advances in discovery approaches, Signal Transduct. Targeted Ther. 6 (1) (2021) 423, https://doi.org/10.1038/s41392-021-00826-7.

[42] M. Chatzopoulou, R.F. Martínez, N.J. Willis, T.D.W. Claridge, F.X. Wilson, G. M. Wynne, S.G. Davies, The Dimroth rearrangement as a probable cause for structural misassignments in imidazo[1,2-a]pyrimidines: a 15N-labelling study and an easy method for the determination of regiochemistry, Tetrahedron 74 (38) (2018) 5280–5288, https://doi.org/10.1016/j.tet.2018.06.033.

[43] R. Jacquier, H. Lopez, G. Maury, Intermediaires dans le rearrangement de dimroth d'imidazo[1,2-a]pyridines, J. Heterocycl. Chem. 10 (1973) 755–762, https://doi.org/10.1002/jhet.5570100513.

[44] S.H. Henderson, F. Sorrell, J. Bennett, O. Fedorov, M.T. Hanley, P.H. Godoi, R. Ruela de Sousa, S. Robinson, A. Ashall-Kelly, I. Hopkins Navratilova, D. S. Walter, J.M. Elkins, S.E. Ward, Discovery and characterization of selective and ligand-efficient DYRK inhibitors, J. Med. Chem. 64 (15) (2021) 11709–11728, https://doi.org/10.1021/acs.jmedchem.1c01115.

[45] S.H. Henderson, F. Sorrell, J. Bennett, M.T. Hanley, S. Robinson, I. Hopkins Navratilova, J.M. Elkins, S.E. Ward, Mining public domain data to develop selective DYRK1A inhibitors, ACS Med. Chem. Lett. 11 (8) (2020) 1620–1626, https://doi.org/10.1021/acsmedchemlett.0c00279.

[46] O. Fedorov, F.H. Niesen, S. Knapp, Kinase inhibitor selectivity profiling using differential scanning fluorimetry, Methods Mol. Biol. 795 (2012) 109–118, https://doi.org/10.1007/978-1-61779-337-0_7.

[47] W. Wei, S. Cherukupalli, L. Jing, X. Liu, P. Zhan, Fsp^3: a new parameter for drug-likeness, Drug Discov. Today 25 (10) (2020) 1839–1845, https://doi.org/10.1016/j.drudis.2020.07.017.